

Object Fidelity Diffusion for Remote Sensing Image Generation

Ziqi Ye^{1,2*}, Shuran Ma^{3*}, Jie Yang², Xiaoyi Yang¹, Ziyang Gong⁴, Xue Yang^{4,†,‡}, Haipeng Wang^{1,†}

¹Fudan University ²Shanghai Innovation Institute ³Xidian University ⁴Shanghai Jiao Tong University
 yezq24@m.fudan.edu.cn, shrma@stu.xidian.edu.cn
<https://github.com/VisionXLab/OF-Diff>

Abstract

High-precision controllable remote sensing image generation is both meaningful and challenging. Existing diffusion models often produce low-fidelity images due to their inability to adequately capture morphological details, which may affect the robustness and reliability of object detection models. To enhance the accuracy and fidelity of generated objects in remote sensing, this paper proposes Object Fidelity Diffusion (OF-Diff), which effectively improves the fidelity of generated objects. Specifically, we are the first to extract the prior shapes of objects based on the layout for diffusion models in remote sensing. Then, we introduce a dual-branch diffusion model with diffusion consistency loss, which can generate high-fidelity remote sensing images without providing real images during the sampling phase. Furthermore, we introduce DDPO to fine-tune the diffusion process, making the generated remote sensing images more diverse and semantically consistent. Comprehensive experiments demonstrate that OF-Diff outperforms state-of-the-art methods in the remote sensing across key quality metrics. Notably, the performance of several polymorphic and small object classes shows significant improvement. For instance, the mAP increases by 8.3%, 7.7%, and 4.0% for airplanes, ships, and vehicles, respectively.

Introduction

Synthesizing high-fidelity, spatially-controllable remote sensing (RS) images is a critical frontier for overcoming the data limitations that hinder downstream perception tasks like object detection (Yang et al. 2021; Zhang et al. 2020; Yang et al. 2019). Current RS generation methods, however, typically rely on either ambiguous text prompts (Khanna et al. 2023; Sebaq and ElHelw 2024) or auxiliary conditions like semantic maps (Sebaq and ElHelw 2024; Tang et al. 2024; Gong et al. 2024; Hu et al. 2025; Jia et al. 2025). While visually plausible, such guidance is fundamentally disconnected from the instance-level ground truth, failing to provide the precise control necessary for effective data augmentation.

In contrast, Layout-to-Image (L2I) generation conditioned on object bounding boxes presents a more robust solution for precise spatial control. While this approach has

*Equal contribution.

†Corresponding author. ‡Project lead.

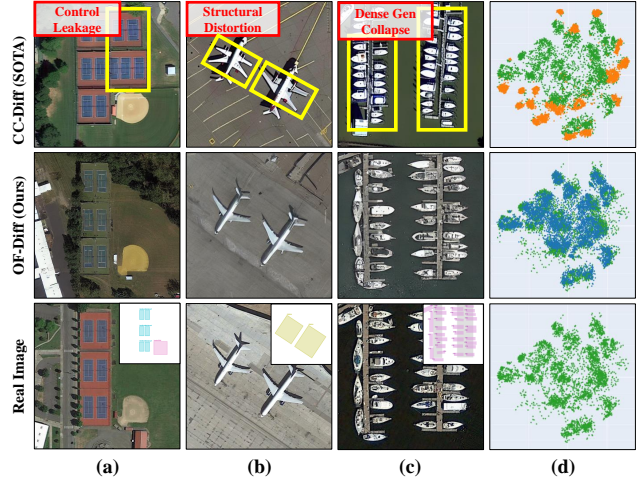


Figure 1: Four critical failure modes in the State-of-the-Art (SOTA) method (CC-Diff): (a) **Control Leakage**: content spills outside the specified layout; (b) **Structural Distortion**: resulting in malformed object morphology; (c) **Dense Generation Collapse**: a loss of control in crowded scenes; and (d) **Feature-level Mismatch**: a distributional drift from real data, visualized by t-SNE. Our OF-Diff (2nd row) effectively resolves these issues.

been extensively developed in the natural image domain with methods like LayoutDiffusion (Zheng et al. 2023) treating it as a multi-modal fusion task, GLIGEN (Li et al. 2023) enabling open-world generation with extra controls, and ODGen (Zhu et al. 2024) decoupling objects for higher controllability, its direct application to RS is non-trivial, due to the unique challenges of RS imagery, such as vast backgrounds, arbitrary object orientations, and dense scenes.

In RS layout-to-image generation, existing methods like AeroGen (Tang et al. 2025) and CC-Diff (Zhang et al. 2024) take different approaches. AeroGen, a coarse layout-conditioned model, suffers from limited spatial and shape control. In contrast, instance-level methods like CC-Diff achieve higher controllability and fidelity by referencing real instances, but this creates heavy dependence on the quality and quantity of real data, limiting generalization and flexibility. We summarize common failure modes (see Figure 1),

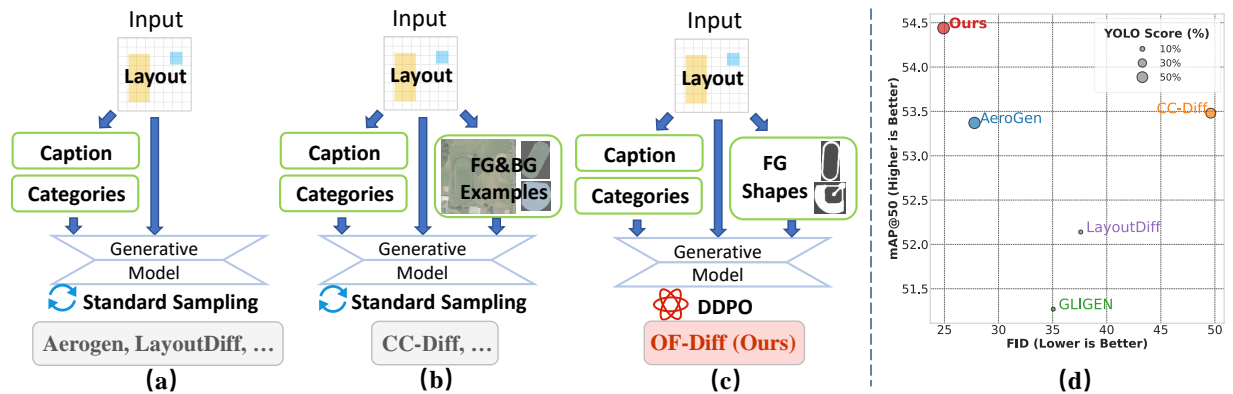


Figure 2: Comparison of OF-Diff with mainstream L2I methods. FG/BG stands for foreground/background. (a) Layout-conditioned baseline. (b) Added instance-based module, limited by quality/quantity of patches from ground truth. (c) OF-Diff enhances fidelity via shape extraction and DDPO, without patch reliance. (d) Results demonstrate superiority.

including control leakage, structural distortion, dense generation collapse, and feature-level mismatch.

These deficiencies significantly degrade the performance on object detection tasks, limiting their practical application in intelligent RS interpretation. In this paper, we introduce **Object Fidelity Diffusion Model (OF-Diff)**. It is designed to improve the shape fidelity and layout consistency of object generation in RS images. As shown in Figure 2, the existing L2I methods are mainly divided into two categories. The first is layout-conditioned baseline, as shown in Figure 2(a), like AeroGen and LayoutDiffusion. The second is the method with instance-based module, as shown in Figure 2(b), like CC-Diff. However, such methods require real instances and images as references during the sampling stage in order to generate high-quality synthetic images. In contrast, OF-Diff only needs to extract the shape of the foreground to generate high-fidelity RS images, as shown in Figure 2(c). In addition, it fine-tunes the diffusion with DDPO, effectively enhancing the performance of downstream tasks for the generated images. The results in Figure 2(d) demonstrates the superiority of OF-Diff over other methods. Our contributions are summarized as follows:

- We introduce OF-Diff, a dual-branch controllable diffusion model with prior shape extraction, which improves generation fidelity while reducing reliance on real images, enhancing practical applicability.
- We propose a controllable generation pipeline that fine-tunes diffusion models with DDPO for remote sensing images, further boosting fidelity and diversity.
- Extensive experiments demonstrate that OF-Diff generates high-fidelity, layout- and shape-consistent images with dense objects, and serves as an effective enhancement for object detection tasks.

Related Work

Advances in Image Generation

Diffusion models (Dhariwal and Nichol 2021; Ho, Jain, and Abbeel 2020; Kingma et al. 2021) have increasingly re-

placed Generative Adversarial Networks (GANs) (Goodfellow et al. 2014; Karras et al. 2021) and Variational Autoencoders (VAEs) (Kingma, Welling et al. 2013; Rezende, Mohamed, and Wierstra 2014) in image synthesis tasks due to their training stability and superior output quality. Recent advances in efficient samplers, such as DDIM (Song, Meng, and Ermon 2021), Euler (Karras et al. 2022), and DPM-Solver (Lu et al. 2022), have further improved the practicality. Latent Diffusion Models (LDMs) (Rombach et al. 2022a), which operate in low-dimensional latent spaces, significantly reduce computational costs while preserving visual fidelity. The success of models like DALL·E2 (Ramesh et al. 2022) and Imagen (Saharia et al. 2022) demonstrates how this paradigm supports training on vast internet-scale datasets. As a result, diffusion-based approaches now provide a strong foundation for high-quality image generation.

Layout-to-Image Generation

Controllable image synthesis primarily includes text-to-image (T2I) and layout-to-image (L2I) generation. While T2I models (Nichol et al. 2022; Ramesh et al. 2022) achieve semantic alignment via textual prompts, L2I methods offer better spatial control. Recent works enhance layout conditioning through layout-as-modality designs (Zheng et al. 2023), gated attention (Li et al. 2023), and instance-wise generation (Wang et al. 2024; Zhou et al. 2024). However, these methods rely solely on coarse layout inputs (e.g., bounding boxes), which lack fine-grained shape information critical for synthesizing morphologically complex objects.

Remote Sensing Image Synthesis

Synthesizing high-fidelity training data is crucial for advancing remote sensing (RS) object detection, a field critical to numerous applications, but often hampered by the scarcity of extensively annotated datasets. Despite its necessity, most generative models for RS imagery, such as DiffusionSat (Khanna et al. 2023) and RSDiff (Sebaq and El-Helw 2024), still rely on coarse semantic guidance. While other approaches leverage diverse control signals (Tang et al.

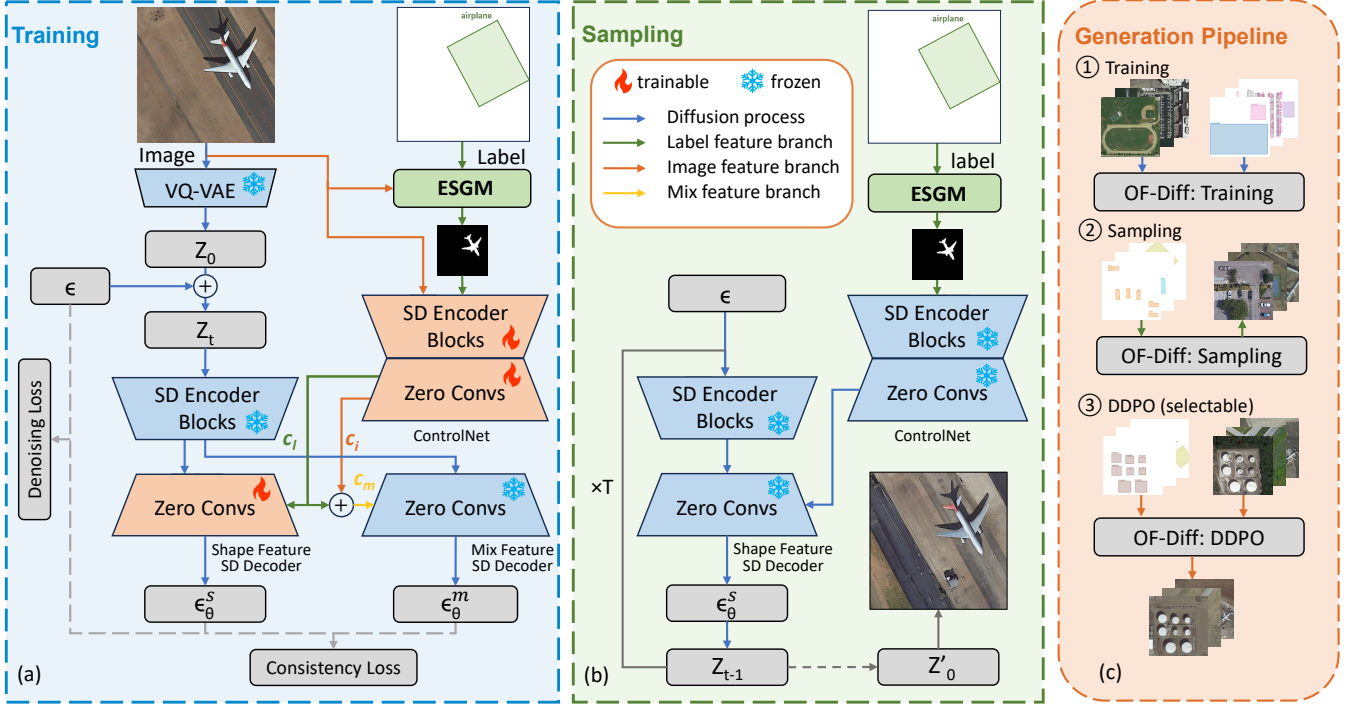


Figure 3: OF-Diff’s overall architecture. (a) During the training phase, the shape features of objects obtained through ESGM and image are feature extracted by Control, and the parameters are updated to the dual-branch stable diffusion. Noisy image Z_t in the latent space is processed through shape feature stable diffusion and Mix feature stable diffusion, generating the noise predictions ϵ_θ^s and ϵ_θ^m . The diffusion consistency loss is calculated by ϵ_θ^s and ϵ_θ^m , and the denoising loss is calculated by ϵ_θ^s and ϵ . (b) During the sampling phase, only label and shape feature stable Diffusion are utilized to generate synthetic images. (c) The pipeline of OF-Diff. DDPO is optional if the generated data is expected to better conform to the distribution of a specific dataset.

2024) like OpenStreetMaps (Espinosa and Crowley 2023), they are generally not optimized for the bounding box format central to object detection. This naturally motivates L2I approaches including AeroGen (Tang et al. 2025) and CC-Diff (Zhang et al. 2024), which have improved spatial accuracy and contextual consistency through layout-mask attention and FG/BG dual re-samplers. However, they suffer from limited controllability and heavy reliance on real data.

Method

Preliminary

Diffusion models (Song, Meng, and Ermon 2021) aim to capture the underlying data distribution $p(x)$ by iteratively reconstructing data from a noisy representation that is initially sampled from a standard normal distribution.

Denoising Diffusion Probabilistic Models (Ho, Jain, and Abbeel 2020) parameterize the model as the function $\epsilon_\theta(x_t, t)$ to predict the noise component of the sample x_t at any time step t . The training objective is to minimize the mean squared error (MSE) loss between the actual noise ϵ and the predicted noise $\epsilon_\theta(x_t, t)$:

$$\mathcal{L} = \mathbb{E}_{x_t, t, \epsilon \sim \mathcal{N}(\mathbf{0}, \mathbf{I})} \left[\|\epsilon_\theta(x_t, t) - \epsilon\|^2 \right]. \quad (1)$$

Stable Diffusion (Rombach et al. 2022a; Qiu et al. 2025) utilizes a pre-trained VQ-VAE (Van Den Oord, Vinyals et al. 2017) to encode images into a lower-dimensional latent space, performing training on the latent representation z_0 . In the context of conditional generation, given a text prompt c_t and task-specific conditions c_f , the diffusion training loss at time step t can be expressed as:

$$\mathcal{L} = \mathbb{E}_{z_t, t, c_t, c_f, \epsilon \sim \mathcal{N}(\mathbf{0}, \mathbf{I})} \left[\|\epsilon - \epsilon_\theta(z_t, t, c_t, c_f)\|^2 \right]. \quad (2)$$

where \mathcal{L} represents the overall learning objective of the complete diffusion model. This objective function is explicitly applied during the fine-tuning of diffusion models in conjunction with ControlNet (Zhang, Rao, and Agrawala 2023).

Architecture of OF-Diff

As illustrated in Figure 3(a), during the training phase of OF-Diff, both the real images and their corresponding labels are needed for diffusion training. First, they are fed into the Enhanced Shape Generation Module (ESGM) for shape extraction, yielding the object mask. Subsequently, the real image and its object mask are fed into ControlNet for feature extraction, resulting in the image feature c_i and the label feature c_l . Second, the input image is first compressed into the

latent space features z_0 by a pre-trained VQ-VAE. Then, it is concatenated with random Gaussian noise ϵ to form z_t . After being injected into the stable diffusion encoder blocks, the feature Z_t is fed into a dual-branch decoder architecture. The two components of this architecture are respectively designated as the shape feature stable diffusion decoder and the mix feature stable diffusion decoder. Third, a weighted summation of c_i and the stop - gradient c_l is carried out to c_m . c_m is defined as:

$$c_m = \frac{n}{N} \cdot c_i + \text{sg}[c_l], \quad (3)$$

where n denotes the current iteration number, and N is the total number of iterations. In order to enable the prediction from the mix feature stable diffusion to serve as an anchor point, guiding the convergence trajectory of the shape stable diffusion and thus improving the morphological fidelity of the image, we adopt a stop-gradient strategy (Chen and He 2021) for c_l when calculating c_m . The loss \mathcal{L}_s and \mathcal{L}_m of shape feature stable diffusion and mix feature stable diffusion are defined as:

$$\mathcal{L}_s = \mathbb{E} \left[\|\epsilon_\theta^s - \epsilon\|^2 \right], \epsilon_\theta^s = \epsilon_\theta(z_t, t, c_t, c_s), \quad (4)$$

$$\mathcal{L}_m = \mathbb{E} \left[\|\epsilon_\theta^m - \epsilon\|^2 \right], \epsilon_\theta^m = \epsilon_\theta(z_t, t, c_t, c_m), \quad (5)$$

To assist the shape feature stable diffusion in breaking away from local minima with low fidelity and migrating towards regions of high fidelity in the parameter space, we introduce a diffusion consistency loss:

$$\mathcal{L}_c = \mathbb{E} \left[\|\epsilon_\theta^m - \text{sg}[\epsilon_\theta^{\text{mix}}]\|^2 \right], \quad (6)$$

The predicted noise ϵ_θ^m from the mix feature stable diffusion is more accurate than ϵ_θ^s predicted by the shape feature stable diffusion, owing to the additional image prior control. Nevertheless, during the sampling process, we do not utilize inputs with real images. Consequently, we employ a stop-gradient operation so that the more accurate ϵ_θ^m can serve as an anchor, guiding the convergence trajectory of the masked diffusion towards high-fidelity local minima in the parameter space. Ultimately, the loss employed to train OF-Diff is defined as:

$$\mathcal{L} = \mathcal{L}_s + \mathcal{L}_m + \mathcal{L}_c, \quad (7)$$

During the sampling phase, as illustrated in Figure 3(b), only the frozen ControlNet and the shape feature stable diffusion are utilized with arbitrary label prior control to synthesize RS images.

Enhanced Shape Generation Module

In natural imagery, perspective and scale changes prevent a unique geometric model for most objects. Conversely, remote-sensing objects display quasi-invariant shapes. For instance, courts are rectangular, chimneys and oil tanks circular, and airplanes bilaterally symmetric with a distinct nose and tail. This shape consistency enables the use of masks to impose strong controllability on image synthesis

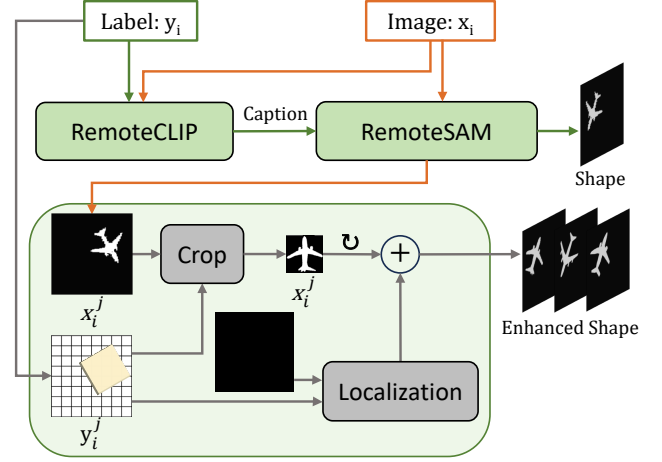


Figure 4: The architecture of Enhanced Shape Generation Module (ESGM).

for remote sensing. To better leverage category labels for object shape extraction, we introduce the Enhanced Shape Generation Module (ESGM, see Figure 4). During the training phase, ESGM uses paired images and labels to generate precise object masks. And at sampling time, it employs learned shape priors to synthesize diverse masks of object shape.

For the given image x_i and its bounding box y_i^j corresponding to category j ($j \in [1, N]$), we first utilize the RemoteCLIP (Liu et al. 2024) to generate a textual description of the object enclosed within the bounding box. With this description and the original image x_i , the RemoteSAM (Yao et al. 2025) then generates the corresponding shape mask x_i^j .

In the shape augmentation phase, we crop x_i^j using its bounding box y_i^j to extract a shape mask x_i^j that contains only the target object. Subsequently, we apply a random rotation to x_i^j and reposition the rotated mask onto a blank canvas using the original bounding box coordinates y_i^j , resulting in a shape-enhanced mask. During the training phase, ESGM can directly obtain the shape of real images. While sampling, ESGM selects enhanced shapes from a mask pool collected during or beyond training, as in common data-efficient practices where segmentation masks are reused or synthesized with minimal impact on generalization. In our setup, we use masks generated during training.

DDPO fine-tuning

To enhance the diversity of the distribution of data generated by the fine-tuned model and maintain better consistency with the distribution of real images (Schulman et al. 2015, 2017), denoising diffusion policy optimization (DDPO) (Black et al. 2023) is applied in the post-training of OF-Diff. DDPO regards the denoising process of the diffusion model as a multi-step Markov decision process (MDP). The mapping relationship is defined as follows:

$$\pi(a_t | s_t) \triangleq p_\theta(\mathbf{x}_{t-1} | \mathbf{x}_t, c) \quad (8)$$

Method	DIOR Dataset					DOTA Dataset				
	FID↓	KID↓	CMMD↓	CAS↑	YOLOScore↑	FID↓	KID↓	CMMD↓	CAS↑	YOLOScore↑
LayoutDiff	37.60	0.015	<u>0.447</u>	70.32	7.01	<u>21.73</u>	<u>0.015</u>	0.288	77.56	21.43
GLIGEN	35.06	0.010	0.622	76.41	6.51	39.79	0.026	0.357	76.19	15.58
AeroGen	<u>27.78</u>	0.013	0.563	81.69	<u>55.38</u>	26.65	0.017	0.298	<u>81.91</u>	44.85
CC-Diff	49.62	0.024	0.685	82.61	42.17	32.40	0.019	<u>0.279</u>	81.63	<u>49.62</u>
Ours	24.92	<u>0.011</u>	0.312	<u>82.55</u>	58.99	20.84	0.014	0.271	83.79	55.68

Table 1: Quantitative comparison with SOTA methods on DIOR and DOTA. We evaluate performance on **generation fidelity** (FID, KID, CMMD) and **layout consistency** (CAS, YOLOScore). OF-Diff demonstrates superior overall performance. The **best** and **second best** results are highlighted. Lower is better (↓), higher is better (↑).

Method	DIOR Dataset			DOTA Dataset		
	mAP	mAP ₅₀	mAP ₇₅	mAP	mAP ₅₀	mAP ₇₅
Baseline	30.51	52.84	32.10	38.09	66.31	38.44
LayoutDiff	29.81	52.14	30.36	38.91	66.75	40.37
GLIGEN	28.48	51.27	29.21	38.84	66.10	40.24
AeroGen	31.53	53.37	33.60	38.45	67.09	39.07
CC-Diff	31.82	53.48	33.97	38.51	66.52	39.02
Ours	32.71	54.44	34.05	40.03	67.89	42.20

Table 2: Trainability (↑) comparison on DIOR and DOTA. ‘Baseline’ denotes accuracy with the unaugmented dataset.

$$P(s_{t+1} | s_t, a_t) \triangleq (\delta_c, \delta_{t-1}, \delta_{\mathbf{x}_{t-1}}) \quad (9)$$

$$\rho_0(s_0) \triangleq (p(c), \delta_T, \mathcal{N}(0, I)) \quad (10)$$

$$R(s_t, a_t) \triangleq \begin{cases} r(\mathbf{x}_0, c), & \text{if } t = 0, \\ 0, & \text{otherwise.} \end{cases} \quad (11)$$

where δ_z denotes the Dirac delta distribution whose probability density is zero everywhere except at z . The symbols s_t and a_t represent the state and action at time t , respectively. Specifically, s_t is defined as the tuple composed of the condition c , the time step t , and the noisy image \mathbf{x}_t at that time, whereas a_t is defined as the noisy image \mathbf{x}_{t-1} from the preceding time step. The policy is denoted by $\pi(a_t | s_t)$, the transition kernel by $P(s_{t+1} | s_t, a_t)$, the initial state distribution by $\rho_0(s_0)$, and the reward function by $R(s_t, a_t)$. To optimize the policy $\pi(a_t | s_t)$ so as to maximize the cumulative reward $\mathbb{E}_{\tau \sim p(\cdot, \cdot | \pi)} \left[\sum_{t=0}^T R(s_t, \mathbf{a}_t) \right]$, the gradient \hat{g} is computed as follows:

$$\hat{g} = \mathbb{E} \left[\sum_{t=0}^T \frac{p_\theta(\mathbf{x}_{t-1} | c, t, \mathbf{x}_t)}{p_{\theta'}(\mathbf{x}_{t-1} | c, t, \mathbf{x}_t)} \cdot r(\mathbf{x}_0, c) \cdot \nabla_\theta \log p_\theta(\mathbf{x}_{t-1} | c, t, \mathbf{x}_t) \right] \quad (12)$$

$$r(\mathbf{x}_0, c) = (KNN(\mathbf{x}_0, \mathbf{x}_0) - \omega KL(\mathbf{x}_0, \mathbf{x}'_0)) \quad (13)$$

The reward functions based on K-Nearest Neighbor (KNN) and KL divergence are introduced, respectively, to optimize the diversity of generated data and the distribution consistency between generated data and real data. ω is the weight parameter, and \mathbf{x}'_0 is the real image in the dataset.

Experiments

Experimental Settings

Datasets.

- **DIOR-R** (Cheng et al. 2022) is a rotated version of the DIOR benchmark (Li et al. 2020), annotated with oriented bounding boxes, 20 categories. We follow the official split, which divides the dataset into training, validation, and test sets with an approximate ratio of 1:1:2. All experiments are trained on the training set and evaluated on the test set.
- **DOTA-v1.0** (Xia et al. 2018) includes 15 common object categories, with 2,806 images and 188,282 instances. This dataset is more challenging due to the presence of numerous dense scenes and small objects. Following MMRotate (Zhou et al. 2022), each image in the training and test sets is cropped into 512×512 tiles, and those without any valid objects are removed. All experiments are conducted on these processed images.

Implementation Details. We train OF-Diff separately on each dataset (DIOR/DOTA), based on the Stable Diffusion 1.5 (Rombach et al. 2022b) pretrained model. Only the ControlNet and shape feature SD decoder are fine-tuned, while all other modules remain frozen. Training is performed using the AdamW optimizer with a learning rate of $1e-5$. The global batch size is set to 64, and training runs for 100 epochs.

Benchmark Methods. We compare our method with state-of-the-art L2I generation models for both remote sensing (AeroGen (Tang et al. 2025), CC-Diff (Zhang et al. 2024)), and natural images (LayoutDiffusion (Zheng et al. 2023), GLIGEN (Li et al. 2023)). For a fair comparison, all models are re-trained using our dataset settings, following their official training details respectively.

Evaluation Metrics. To more comprehensively evaluate the effectiveness of OF-Diff, we adopt a total of 13 metrics spanning 4 different evaluation aspects.



Figure 5: Qualitative results on DIOR and DOTA. OF-Diff is more realistic and fidelity compared to other methods.

- **Generation Fidelity.** We use **FID** (Heusel et al. 2017) and **KID** (Bińkowski et al. 2018) to assess perceptual quality, along with **CMMD** (Jayasumana et al. 2024), which measures CLIP feature distances between generated and real images to evaluate layout alignment.
- **Layout Consistency.** We report **CAS** (Ravuri and Vinyals 2019) using a pretrained classifier to assess object recognizability, and **YOLOScore** by applying a pretrained Oriented R-CNN (Xie et al. 2021) (w/ Swin Transformer backbone (Liu et al. 2021), MMRotate) to generated images for instance-level consistency.
- **Shape Fidelity.** To assess the geometric quality of generated instances, we perform pairwise comparisons with ground-truth shapes. Each instance pair is cropped, resized to 64×64 , and converted to edge maps. We compute five metrics: **IoU**, **Dice**, Chamfer Distance (**CD**), Hausdorff Distance (**HD**), and **SSIM** (Wang et al. 2004).
- **Downstream Utility.** We train a detector on mixed real and generated images and report **mAP₅₀**, **mAP₇₅**, and overall **mAP** on real test data using Oriented R-CNN (Swin backbone) with a batch size of 24 on $8 \times$ NVIDIA

4090 GPUs.

Qualitative Results

Comparative Results. Figure 5 compares the generation results of OF-Diff with other methods. OF-Diff not only generates more realistic images but also has the best controllability. For instance, in the first two cases, OF-Diff successfully controlled the number and layout information of the generated objects. The third and fourth cases demonstrate the accuracy of OF-Diff in generating small targets, which other algorithms fail to do accurately. The last case shows the superiority of OF-Diff over other algorithms when generating objects with complex shapes such as airplane.

Diversity Results. Figure 6 shows that the images generated by OF-Diff consistently present plausible textures and realistic object shapes. For instance, airplanes rendered at different orientations maintain coherent semantic relationships with their surrounding environments. Even in small-object scenes (some of which are grayscale remote-sensing images from the DOTA dataset), OF-Diff can still generate visually faithful and geometrically accurate results.

Method	Dataset	IoU \uparrow	Dice \uparrow	CD \downarrow	HD \downarrow	SSIM \uparrow
LayoutDiff	DIOR	0.0497	0.0908	12.037	25.962	0.1667
GLIGEN		0.055	0.1002	12.257	25.850	0.1652
AeroGen		0.0855	0.153	8.209	20.314	0.2142
CC-Diff		0.0891	0.1582	8.0909	20.066	0.1963
Ours		0.1009	0.1763	7.6579	19.459	0.2691
LayoutDiff	DOTA	0.0402	0.0748	15.229	30.202	0.2194
GLIGEN		0.0645	0.1182	10.432	23.196	0.1967
AeroGen		0.0863	0.1536	8.1386	20.687	0.2261
CC-Diff		0.0692	0.1255	9.6226	21.247	0.2171
Ours		0.1205	0.2045	6.6317	17.311	0.2938

Table 3: Object-Shape Fidelity on Canny Edge Maps. We measure the morphological similarity between generated and ground-truth instances by computing IoU, DICE, Chamfer Distance (CD), Hausdorff Distance (HD), and SSIM.

Method	Unknown Layout during Training					
	FID \downarrow	KID \downarrow	CMMD \downarrow	CAS \uparrow	YOLO Score \uparrow	mAP \uparrow
LayoutDiff	44.58	0.018	0.539	29.34	10.37	53.07
GLIGEN	39.56	<u>0.013</u>	0.444	66.36	2.13	52.68
AeroGen	<u>28.62</u>	<u>0.013</u>	<u>0.276</u>	<u>80.78</u>	46.36	<u>55.11</u>
CC-Diff	49.92	0.024	0.513	78.01	51.74	53.72
Ours	24.18	0.012	0.271	83.34	<u>49.59</u>	56.65

Table 4: Quantitative comparison on the unknown layout dataset during training (DIOR Val).

Quantitative Results

Generation Fidelity and Consistency. We compared OF-Diff with state-of-the-art generation methods in remote sensing, including layoutDiffusion (Zheng et al. 2023), GLIGEN (Li et al. 2023), AeroGen (Tang et al. 2025), and CC-Diff (Zhang et al. 2024). The performance of these methods is reported in Table 1. OF-Diff achieved nearly the best performance in both generation fidelity metrics (FID, KID, CMMD) and layout consistency metrics, especially on the DOTA dataset.

Trainability of Object Detection. Following the data enhancement protocol in (Chen et al. 2023), we double the training samples using OF-Diff and assess detection results with the expanded dataset. As shown in Table 2, OF-Diff performs the best on both DIOR and DOTA. Specifically, OF-Diff improves mAP by 2.2% on DIOR and 1.94% on DOTA compared to baseline. Notably, the performance of several polymorphic and small object classes shows significant improvement. According to Figure 7, the AP $_{50}$ increases by 8.3%, 7.7%, and 4.0% for airplane, ship, and vehicle on DIOR, and 7.1%, 5.9% and 4.4% for swimming pool, small vehicle, and large vehicle on DOTA.

Object-Shape Fidelity. We measure the morphological similarity between the generated instances and ground truth by calculating the Intersection over Union (IoU), DICE coefficient, Chamfer distance (CD), Hausdorff distance (HD), and Structural Similarity Index (SSIM), based on the Canny



Figure 6: The diversity of different results from the same OF-Diff model.

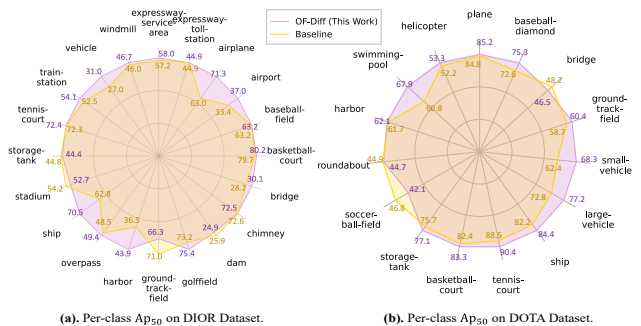


Figure 7: AP $_{50}$ on DIOR and DOTA.

Edge Map. As shown in Table 3, the results demonstrate that OF-Diff attains state-of-the-art performance in all evaluation metrics for object-shape fidelity. Specifically, we first convert the rotated bounding box (R-Box) to a horizontal bounding box (H-Box) and crop the instance with a 20% padding to ensure the full object is captured. The cropped patches are then resized to 64×64 pixels, and their shapes are extracted using cv2.Canny. For a detailed qualitative comparison, Figure 9 visualizes the instance patches and their corresponding edge maps from different methods. Each image set is ordered as follows: Ground Truth, OF-Diff, AeroGen, CC-Diff, GLIGEN, and LayoutDiff, demonstrating our method’s superior ability to adhere to object shapes.

Adaptability of Unknown Layout. To better demonstrate the scalability of these methods, we also generate images based on the unknown layouts during the training phase. According to Table 4, for unknown layout, OF-Diff performs well in terms of generation fidelity, layout consistency, and trainability. In downstream tasks, OF-Diff still delivers a 1.54% mAP gain over the second-best method.

The Detailed Results of Downstream. Table 6 and 7 report the average precision (AP) obtained by the competing generative methods over multiple categories in the downstream tasks. From Tables 6, it can be observed that OF-Diff (ours) achieves a clear advantage in several categories. For instance, OF-Diff achieves superior performance on Airplane (71.3%), Golf Field (75.4%) and Ship (70.5%), with improvements of approximately 5% to 10% over the second-

ESGM	DCLoss	DDPO	CAS \uparrow	YOLOScore \uparrow	mAP ₅₀ \uparrow
\times	\times	\times	80.27	41.20	52.13
\checkmark	\times	\times	82.16	55.08	52.76
\times	\checkmark	\times	81.57	46.27	53.14
\times	\checkmark	\checkmark	81.91	47.74	53.21
\checkmark	\checkmark	\times	82.30	57.83	54.31
\checkmark	\checkmark	\checkmark	82.55	58.99	54.44

Table 5: Ablation study: impact of ESGM, DCLoss, and DDPO on semantic consistency (CAS) and downstream trainability (YOLOScore and mAP₅₀).



Figure 8: The influence of caption on the generation of images in terms of being more realistic and more aesthetically pleasing.

best method. For a few other categories, OF-Diff does not deliver the top AP, yet the gap to the best result remains marginal. Table 7 shows that, on the DOTA dataset, OF-Diff obtains the highest AP in roughly half of all categories and still delivers notable gains in categories such as Small-vehicle (68.3%), Ship (84.4%) and Swimming-pool (67.9%).

Ablation Study

We assessed the impact of different modules on image generation semantic consistency and downstream trainability by OF-Diff in Table 5. We found that the input of captions would affect the fidelity of image generation. Images generated with captions are more in line with semantic consistency and human aesthetics, but the fidelity of these images decreases. This is equivalent to the data distribution deviating from the real dataset and being more inclined towards the data distribution during pre-training. Therefore, the ablation experiments for each module were conducted based on the absence of caption input. The contribution of each module to the enhancement of image generation fidelity is evaluated by incorporating additional components into the diffusion model with dual-branch. DDPO indicates whether to fine-tune the trained diffusion model through reinforcement learning. Results show that Enhanced Shape Generation Module (ESGM), Diffusion Consistency Loss (DCLoss) and the DDPO based on KNN and KL Divergence effectively improve the performance metrics. Notably,

ESGM can substantially improve the YOLOScore by over 10%.

Discussion

As shown in Figure 8, the inclusion of additional captions as input has a significant impact on the outcomes of image generation. Specifically, incorporating captions enhances the aesthetic appeal of the generated images, resulting in richer and more visually pleasing color compositions. However, this improvement comes at a cost: similar to CC-Diff, it leads to a deviation of the generated data distribution from that of the original real data. In contrast, when no additional captions are provided as input, although the generated images may appear less aesthetically refined, their data distribution remains closer to that of real images. Furthermore, experimental results demonstrate that this approach yields superior performance in terms of image quality metrics and downstream task effectiveness.

According to the current experimental results, adding the DDPO strategy does not simultaneously outperform previous results on all metrics. Using reinforcement learning strategies can indeed improve the performance of downstream tasks, but it does not necessarily improve the quality of image generation simultaneously. In other words, reinforcement learning strategies can also purposefully improve the quality of image generation, but this may come at the cost of not improving the performance of downstream tasks.

Limitations

The proposed OF-Diff injects object shape masks extracted from the image layout as controllable conditions into the diffusion model, which effectively enhances object fidelity and improves the generation of small objects. However, this also makes the model heavily dependent on the quality of the extracted shape masks. If the obtained masks are already distorted, the resulting generated images will likewise fail to achieve satisfactory quality.

Conclusion

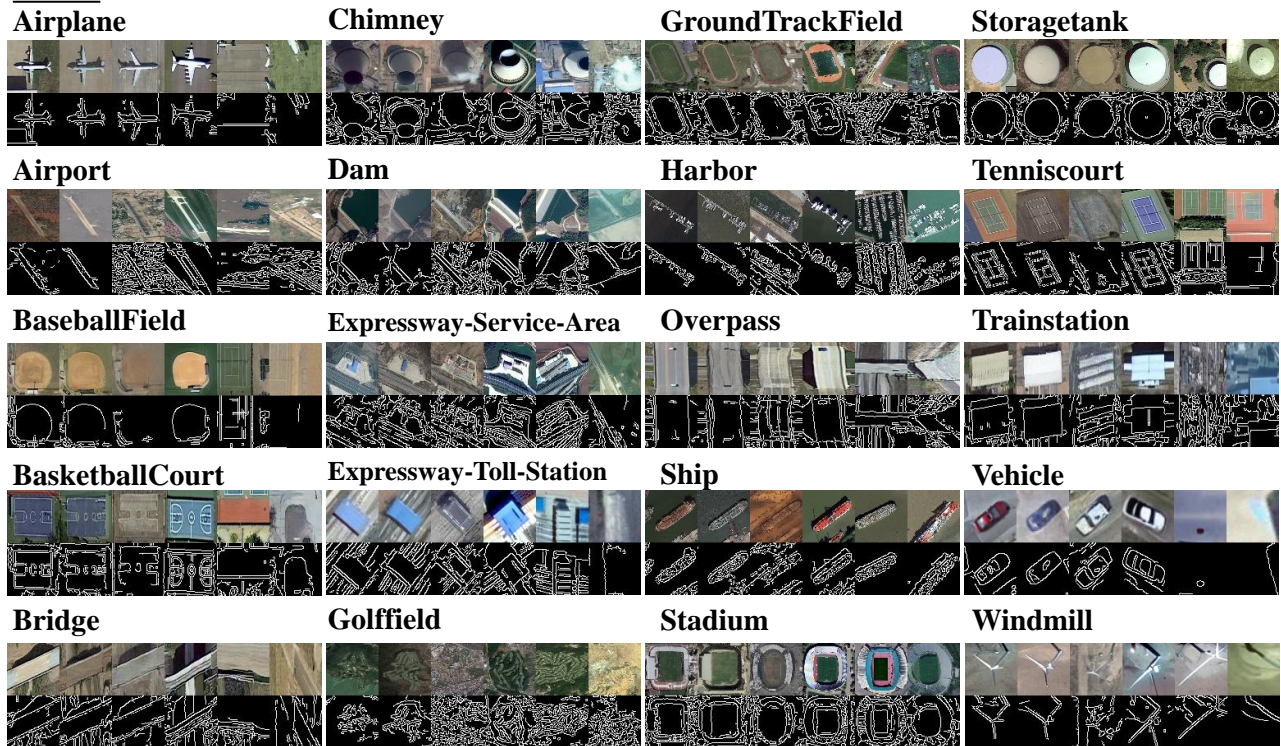
Existing image generation methods struggle to precisely generate dense small objects and those with complex shapes, such as numerous small vehicles and airplanes in remote sensing images. To address this, we introduce OF-Diff, a dual-branch controllable diffusion model with prior shapes extraction and DDPO. During the training phase, we extract the prior shape of objects to enhance controllability and use a dual-branch diffusion with parameter sharing to improve the model’s learning ability for real images. Therefore, in the sampling phase, OF-Diff can generate images with high fidelity without real images as references. Finally, we fine-tune the diffusion by DDPO that combines KNN and KL divergence to make the synthesized images more realistic and consistent. Extensive experiments demonstrate the effectiveness and superiority of OF-Diff in generating small and difficult objects with complex structures and dense scenes in remote sensing.

References

- Biríkowski, M.; Sutherland, D. J.; Arbel, M.; and Gretton, A. 2018. Demystifying MMD GANs. In *International Conference on Learning Representations*.
- Black, K.; Janner, M.; Du, Y.; Kostrikov, I.; and Levine, S. 2023. Training diffusion models with reinforcement learning. *arXiv preprint arXiv:2305.13301*.
- Chen, K.; Xie, E.; Chen, Z.; Wang, Y.; Hong, L.; Li, Z.; and Yeung, D.-Y. 2023. GeoDiffusion: Text-Prompted Geometric Control for Object Detection Data Generation.
- Chen, X.; and He, K. 2021. Exploring Simple Siamese Representation Learning. In *2021 IEEE/CVF Conference on Computer Vision and Pattern Recognition (CVPR)*.
- Cheng, G.; Wang, J.; Li, K.; Xie, X.; Lang, C.; Yao, Y.; and Han, J. 2022. Anchor-free oriented proposal generator for object detection. *IEEE Transactions on Geoscience and Remote Sensing*, 60: 1–11.
- Dhariwal, P.; and Nichol, A. 2021. Diffusion models beat gans on image synthesis. *Advances in neural information processing systems*, 34: 8780–8794.
- Espinosa, M.; and Crowley, E. J. 2023. Generate your own scotland: Satellite image generation conditioned on maps. *arXiv preprint arXiv:2308.16648*.
- Gong, Z.; Wei, Z.; Wang, D.; Ma, X.; Chen, H.; Jia, Y.; Deng, Y.; Ji, Z.; Zhu, X.; Yokoya, N.; et al. 2024. Crossearth: Geospatial vision foundation model for domain generalizable remote sensing semantic segmentation. *arXiv preprint arXiv:2410.22629*.
- Goodfellow, I. J.; Pouget-Abadie, J.; Mirza, M.; Xu, B.; Warde-Farley, D.; Ozair, S.; Courville, A.; and Bengio, Y. 2014. Generative adversarial nets. *Advances in neural information processing systems*, 27.
- Heusel, M.; Ramsauer, H.; Unterthiner, T.; Nessler, B.; and Hochreiter, S. 2017. Gans trained by a two time-scale update rule converge to a local nash equilibrium. *Advances in neural information processing systems*, 30.
- Ho, J.; Jain, A.; and Abbeel, P. 2020. Denoising diffusion probabilistic models. *Advances in neural information processing systems*, 33: 6840–6851.
- Hu, X.; Gong, Z.; Wang, Y.; Jia, Y.; Luo, G.; and Yang, X. 2025. Earth-Adapter: Bridge the Geospatial Domain Gaps with Mixture of Frequency Adaptation. *arXiv preprint arXiv:2504.06220*.
- Jayasumana, S.; Ramalingam, S.; Veit, A.; Glasner, D.; Chakrabarti, A.; and Kumar, S. 2024. Rethinking fid: Towards a better evaluation metric for image generation. In *Proceedings of the IEEE/CVF Conference on Computer Vision and Pattern Recognition*, 9307–9315.
- Jia, Y.; Marsocci, V.; Gong, Z.; Yang, X.; Vergauwen, M.; and Nascetti, A. 2025. Can Generative Geospatial Diffusion Models Excel as Discriminative Geospatial Foundation Models? *arXiv preprint arXiv:2503.07890*.
- Karras, T.; Aittala, M.; Aila, T.; and Laine, S. 2022. Elucidating the design space of diffusion-based generative models. *Advances in neural information processing systems*, 35: 26565–26577.
- Karras, T.; Aittala, M.; Laine, S.; Härkönen, E.; Hellsten, J.; Lehtinen, J.; and Aila, T. 2021. Alias-free generative adversarial networks. *Advances in neural information processing systems*, 34: 852–863.
- Khanna, S.; Liu, P.; Zhou, L.; Meng, C.; Rombach, R.; Burke, M.; Lobell, D.; and Ermon, S. 2023. Diffusionsat: A generative foundation model for satellite imagery. *arXiv preprint arXiv:2312.03606*.
- Kingma, D.; Salimans, T.; Poole, B.; and Ho, J. 2021. Variational diffusion models. *Advances in neural information processing systems*, 34: 21696–21707.
- Kingma, D. P.; Welling, M.; et al. 2013. Auto-encoding variational bayes.
- Li, K.; Wan, G.; Cheng, G.; Meng, L.; and Han, J. 2020. Object detection in optical remote sensing images: A survey and a new benchmark. *ISPRS journal of photogrammetry and remote sensing*, 159: 296–307.
- Li, Y.; Liu, H.; Wu, Q.; Mu, F.; Yang, J.; Gao, J.; Li, C.; and Lee, Y. J. 2023. Gligen: Open-set grounded text-to-image generation. In *Proceedings of the IEEE/CVF conference on computer vision and pattern recognition*, 22511–22521.
- Liu, F.; Chen, D.; Guan, Z.; Zhou, X.; Zhu, J.; Ye, Q.; Fu, L.; and Zhou, J. 2024. Remoteclip: A vision language foundation model for remote sensing. *IEEE Transactions on Geoscience and Remote Sensing*, 62: 1–16.
- Liu, Z.; Lin, Y.; Cao, Y.; Hu, H.; Wei, Y.; Zhang, Z.; Lin, S.; and Guo, B. 2021. Swin transformer: Hierarchical vision transformer using shifted windows. In *Proceedings of the IEEE/CVF international conference on computer vision*, 10012–10022.
- Lu, C.; Zhou, Y.; Bao, F.; Chen, J.; Li, C.; and Zhu, J. 2022. Dpm-solver: A fast ode solver for diffusion probabilistic model sampling in around 10 steps. *Advances in neural information processing systems*, 35: 5775–5787.
- Nichol, A. Q.; Dhariwal, P.; Ramesh, A.; Shyam, P.; Mishkin, P.; Mcgrew, B.; Sutskever, I.; and Chen, M. 2022. GLIDE: Towards Photorealistic Image Generation and Editing with Text-Guided Diffusion Models. In *International Conference on Machine Learning*, 16784–16804. PMLR.
- Qiu, K.; Gao, Z.; Zhou, Z.; Sun, M.; and Guo, Y. 2025. Noise-Consistent Siamese-Diffusion for Medical Image Synthesis and Segmentation. In *Proceedings of the Computer Vision and Pattern Recognition Conference*, 15672–15681.
- Ramesh, A.; Dhariwal, P.; Nichol, A.; Chu, C.; and Chen, M. 2022. Hierarchical text-conditional image generation with clip latents. *arXiv preprint arXiv:2204.06125*, 1(2): 3.
- Ravuri, S.; and Vinyals, O. 2019. Classification accuracy score for conditional generative models. *Advances in neural information processing systems*, 32.
- Rezende, D. J.; Mohamed, S.; and Wierstra, D. 2014. Stochastic backpropagation and approximate inference in deep generative models. In *International conference on machine learning*, 1278–1286. PMLR.

- Rombach, R.; Blattmann, A.; Lorenz, D.; Esser, P.; and Ommer, B. 2022a. High-Resolution Image Synthesis with Latent Diffusion Models. In *2022 IEEE/CVF Conference on Computer Vision and Pattern Recognition (CVPR)*.
- Rombach, R.; Blattmann, A.; Lorenz, D.; Esser, P.; and Ommer, B. 2022b. High-Resolution Image Synthesis With Latent Diffusion Models. In *Proceedings of the IEEE/CVF Conference on Computer Vision and Pattern Recognition (CVPR)*, 10684–10695.
- Saharia, C.; Chan, W.; Saxena, S.; Li, L.; Whang, J.; Denton, E. L.; Ghasemipour, K.; Gontijo Lopes, R.; Karagol Ayan, B.; Salimans, T.; et al. 2022. Photorealistic text-to-image diffusion models with deep language understanding. *Advances in neural information processing systems*, 35: 36479–36494.
- Schulman, J.; Levine, S.; Abbeel, P.; Jordan, M.; and Moritz, P. 2015. Trust region policy optimization. In *International conference on machine learning*, 1889–1897. PMLR.
- Schulman, J.; Wolski, F.; Dhariwal, P.; Radford, A.; and Klimov, O. 2017. Proximal policy optimization algorithms. *arXiv preprint arXiv:1707.06347*.
- Sebaq, A.; and ElHelw, M. 2024. Rsdiff: Remote sensing image generation from text using diffusion model. *Neural Computing and Applications*, 36(36): 23103–23111.
- Song, J.; Meng, C.; and Ermon, S. 2021. Denoising Diffusion Implicit Models. In *International Conference on Learning Representations*.
- Tang, D.; Cao, X.; Hou, X.; Jiang, Z.; Liu, J.; and Meng, D. 2024. Crs-diff: Controllable remote sensing image generation with diffusion model. *IEEE Transactions on Geoscience and Remote Sensing*.
- Tang, D.; Cao, X.; Wu, X.; Li, J.; Yao, J.; Bai, X.; Jiang, D.; Li, Y.; and Meng, D. 2025. AeroGen: Enhancing remote sensing object detection with diffusion-driven data generation. In *Proceedings of the Computer Vision and Pattern Recognition Conference*, 3614–3624.
- Van Den Oord, A.; Vinyals, O.; et al. 2017. Neural discrete representation learning. *Advances in neural information processing systems*, 30.
- Wang, X.; Darrell, T.; Rambhatla, S. S.; Girdhar, R.; and Misra, I. 2024. Instancediffusion: Instance-level control for image generation. In *Proceedings of the IEEE/CVF conference on computer vision and pattern recognition*, 6232–6242.
- Wang, Z.; Bovik, A. C.; Sheikh, H. R.; and Simoncelli, E. P. 2004. Image quality assessment: from error visibility to structural similarity. *IEEE transactions on image processing*, 13(4): 600–612.
- Xia, G.-S.; Bai, X.; Ding, J.; Zhu, Z.; Belongie, S.; Luo, J.; Datcu, M.; Pelillo, M.; and Zhang, L. 2018. DOTA: A Large-Scale Dataset for Object Detection in Aerial Images. In *The IEEE Conference on Computer Vision and Pattern Recognition (CVPR)*.
- Xie, X.; Cheng, G.; Wang, J.; Yao, X.; and Han, J. 2021. Oriented R-CNN for Object Detection. In *Proceedings of the IEEE/CVF International Conference on Computer Vision (ICCV)*, 3520–3529.
- Yang, X.; Yan, J.; Feng, Z.; and He, T. 2021. R3det: Refined single-stage detector with feature refinement for rotating object. In *Proceedings of the AAAI conference on artificial intelligence*, volume 35, 3163–3171.
- Yang, X.; Yang, J.; Yan, J.; Zhang, Y.; Zhang, T.; Guo, Z.; Sun, X.; and Fu, K. 2019. SCRDet: Towards More Robust Detection for Small, Cluttered and Rotated Objects. In *Proceedings of the IEEE/CVF International Conference on Computer Vision (ICCV)*.
- Yao, L.; Liu, F.; Chen, D.; Zhang, C.; Wang, Y.; Chen, Z.; Xu, W.; Di, S.; and Zheng, Y. 2025. RemoteSAM: Towards Segment Anything for Earth Observation. *arXiv preprint arXiv:2505.18022*.
- Zhang, L.; Rao, A.; and Agrawala, M. 2023. Adding conditional control to text-to-image diffusion models. In *Proceedings of the IEEE/CVF international conference on computer vision*, 3836–3847.
- Zhang, M.; Liu, Y.; Liu, Y.; Zhao, Y.; and Ye, Q. 2024. CC-Diff: enhancing contextual coherence in remote sensing image synthesis. *arXiv preprint arXiv:2412.08464*.
- Zhang, X.; Han, L.; Han, L.; and Zhu, L. 2020. How well do deep learning-based methods for land cover classification and object detection perform on high resolution remote sensing imagery? *Remote Sensing*, 12(3): 417.
- Zheng, G.; Zhou, X.; Li, X.; Qi, Z.; Shan, Y.; and Li, X. 2023. Layoutdiffusion: Controllable diffusion model for layout-to-image generation. In *Proceedings of the IEEE/CVF Conference on Computer Vision and Pattern Recognition*, 22490–22499.
- Zhou, D.; Li, Y.; Ma, F.; Zhang, X.; and Yang, Y. 2024. MIGC: Multi-Instance Generation Controller for Text-to-Image Synthesis. In *Proceedings of the IEEE/CVF Conference on Computer Vision and Pattern Recognition (CVPR)*, 6818–6828.
- Zhou, Y.; Yang, X.; Zhang, G.; Wang, J.; Liu, Y.; Hou, L.; Jiang, X.; Liu, X.; Yan, J.; Lyu, C.; et al. 2022. Mmrotate: A rotated object detection benchmark using pytorch. In *Proceedings of the 30th ACM International Conference on Multimedia*, 7331–7334.
- Zhu, J.; Li, S.; Liu, Y. A.; Yuan, J.; Huang, P.; Shan, J.; and Ma, H. 2024. Odgen: Domain-specific object detection data generation with diffusion models. *Advances in Neural Information Processing Systems*, 37: 63599–63633.

DIOR



DOTA

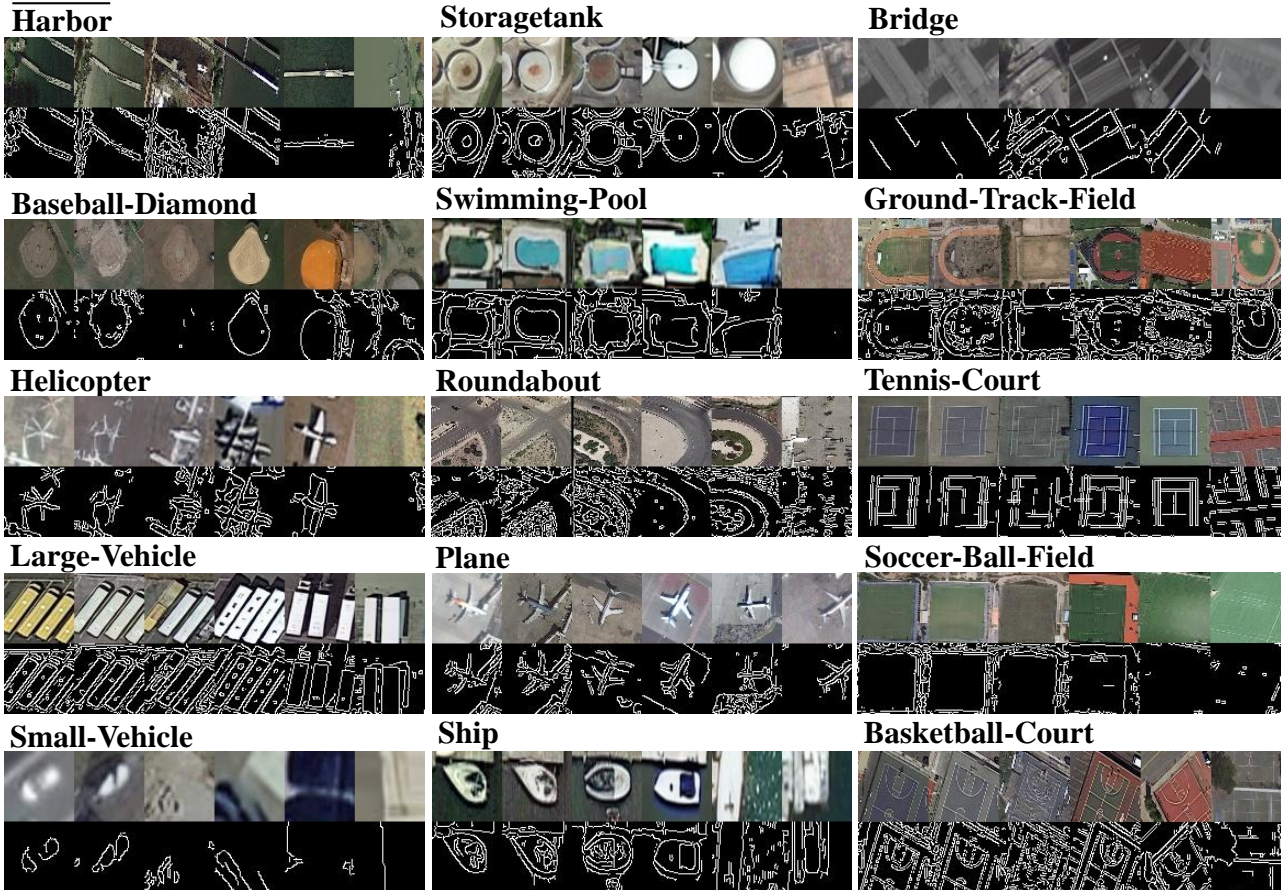


Figure 9: Comparison of generated instance patches and their Canny edge maps for the same bbox on the DIOR and DOTA dataset. Each image set is ordered as follows: Ground Truth, OF-Diff, AeroGen, CC-Diff, GLIGEN, and LayoutDiff.

Method	DIOR Dataset									
	Expressway Service-area	Expressway toll-station	Airplane	Airport	Baseball field	Basketball court	Bridge	Chimney	Dam	Golf Field
LayoutDiff	53.1	44.8	62.8	29.4	63.2	79.6	25.9	72.6	22.4	69.3
GLIGEN	52.7	44.8	62.6	26.7	63.0	79.6	25.2	72.6	19.5	67.4
AeroGen	58.1	45.2	63.1	32.7	63.4	81.0	29.5	72.6	21.1	69.1
CC-Diff	53.5	45.1	62.9	38.4	63.3	79.9	29.3	72.7	27.6	70.5
Ours	58.0	44.9	71.3	37.0	63.2	80.2	30.1	72.5	24.9	75.4

Method	DIOR Dataset									
	Ground Track-field	Harbor	Overpass	Ship	Stadium	Storage Tank	Tennis Court	Trainstation	Vehicle	Windmill
LayoutDiff	71.2	32.8	43.9	62.9	59.0	52.5	72.4	52.1	26.9	46.0
GLIGEN	70.1	30.3	45.8	62.8	56.8	52.0	72.5	49.0	26.9	45.3
AeroGen	71.0	42.7	50.7	62.9	56.6	44.5	72.5	52.6	31.4	46.7
CC-Diff	64.6	43.1	49.0	63.0	61.7	44.7	72.4	54.4	27.0	46.5
Ours	66.3	43.9	49.4	70.5	52.7	44.4	72.4	54.1	31.0	46.7

Table 6: Detailed downstream trainability results (measured by average precision) on the DIOR dataset.

Method	DOTA Dataset							
	Plane	Baseball-diamond	Bridge	Ground Track-field	Small-vehicle	Large-vehicle	Ship	Tennis-court
LayoutDiff	80.4	74.2	48.8	59.9	62.9	72.7	82.5	89.6
GLIGEN	87.0	72.9	47.3	56.4	63.7	73.1	82.7	90.1
AeroGen	86.1	77.3	48.6	58.6	64.5	78.1	82.5	83.3
CC-Diff	87.2	73.4	47.1	57.8	64.3	73.9	82.6	89.2
Ours	85.2	75.3	46.5	60.4	68.3	77.2	84.4	90.4

Method	DOTA Dataset						
	Basketball-court	Storage-tank	Soccer-ball-field	Roundabout	Harbor	Swimming-pool	Helicopter
LayoutDiff	78.9	76.3	46.3	47.6	60.9	62.1	57.9
GLIGEN	79.6	76.5	42.2	43.1	60.7	62.3	53.8
AeroGen	77.3	79.9	44.8	46.6	59.4	62.6	56.4
CC-Diff	79.0	82.7	42.7	43.1	58.9	62.7	52.9
Ours	83.3	77.1	42.1	44.7	62.1	67.9	53.3

Table 7: Detailed downstream trainability results (measured by average precision) on the DOTA dataset.



Figure 10: Additional qualitative results on DIOR and DOTA. The results demonstrate that OF-Diff has certain superiority and accuracy in generating small objects, and it also has an advantage in generating the shapes of objects. For instance, the aircraft target in the third row is generated more accurately by OF-Diff, with a more realistic structure. The small vehicles in the fourth and fifth rows and the large vehicle in the sixth row are also more accurately generated. Additionally, the small ship in the seventh row is generated with greater accuracy.